ACS NANO
Cite This: ACS Nano 2020, 14, 1379−1389
www.acsnano.org

ARTICLE

Forward and Backward Switching of Nonlinear Unidirectional Emission from GaAs Nanoantennas

Lei Xu,[†,⊥] Grégoire Saerens,[‡,⊥] Maria Timofeeva,[‡] Daria A. Smirnova,[¶,§] Irina Volkovskaya,[§] Mykhaylo Lysevych,[∥] Rocio Camacho-Morales,[¶] Marcus Cai,[¶] Khosro Zangeneh Kamali,[¶] Lujun Huang,[†] Fouad Karouta,[∥] Hark Hoe Tan,[∥] Chennupati Jagadish,[∥] Andrey E. Miroshnichenko,*[,†] Rachel Grange,*[,‡] Dragomir N. Neshev,*[,¶] and Mohsen Rahmani[¶]

[†]School of Engineering and Information Technology, University of New South Wales, Canberra, ACT 2600, Australia
[‡]Optical Nanomaterial Group, Institute for Quantum Electronics, Department of Physics, ETH Zurich, 8093 Zurich, Switzerland
[¶]Nonlinear Physics Centre, Research School of Physics, The Australian National University, Canberra, ACT 2601, Australia
[§]Institute of Applied Physics, Russian Academy of Sciences, Nizhny Novgorod 603950, Russia
[∥]Department of Electronic Materials Engineering, Research School of Physics, The Australian National University, Canberra, ACT 2601, Australia

Supporting Information

ABSTRACT: **High-index III−V semiconductor nanoantennas have gained great attention for enhanced nonlinear light−matter interactions, in the past few years. However, the complexity of nonlinear emission profiles imposes severe constraints on practical applications, such as in optical communications and integrated optoelectronic devices. These complexities include the lack of unidirectional nonlinear emission and the severe challenges in switching between forward and backward emissions, due to the structure of the susceptibility tensor of the III−V nanoantennas. Here, we propose a solution to both issues via engineering the nonlinear tensor of the nanoantennas. The special nonlinear tensorial properties of zinc-blende material can be used to engineer the nonlinear characteristics via growing the nanoantennas along different crystalline orientations. Based on the nonlinear multipolar effect, we have designed and fabricated (110)-grown GaAs nanoantennas, with engineered tensorial properties, embedded in a transparent low-index material. Our technique provides an approach not only for unidirectional second-harmonic generation (SHG) forward or backward emission but also for switching from one to another. Importantly, switching the SHG emission directionality is obtained only by rotating the polarization of the incident light, without the need for physical variation of the antennas or the environment. This characteristic is an advantage, as compared to other nonlinear nanoantennas, including (100)- and (111)-grown III−V counterparts or silicon and germanium nanoantennas. Indeed, (110)-GaAs nanoantennas allow for engineering the nonlinear nanophotonic systems including nonlinear "Huygens metasurfaces" and offer exciting opportunities for various nonlinear nanophotonics technologies, such as nanoscale light routing and light sources, as well as multifunctional flat optical elements.**

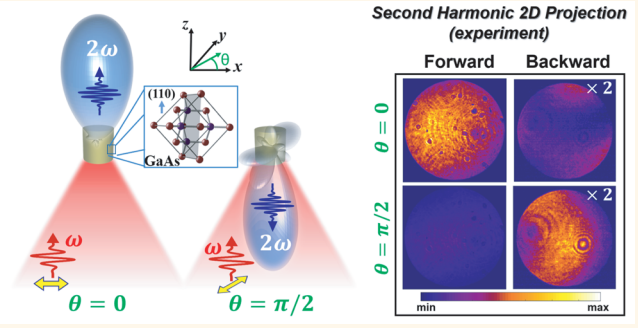

KEYWORDS: *high-index nanoantennas, unidirectional emission, III−V semiconductors, second harmonic generation, Mie resonance, nonlinear tensor*

Nonlinear nanophotonics permits the generation of light at new frequencies and the control of photon−photon interactions at a subwavelength scale by employing nonlinear properties of optical materials.[1] It facilitates nonlinear light−matter interactions such as frequency conversion,[2−4] wave mixing,[5−8] and all-optical switching.[9−11] Currently, nonlinear nanophotonics is a rapidly developing research field with benefiting applications including chip-based light sources,[12] nanolasers,[13,14] imaging, and

Received: September 8, 2019
Accepted: December 26, 2019
Published: December 26, 2019

DOI: 10.1021/acsnano.9b07117
ACS Nano 2020, 14, 1379−1389

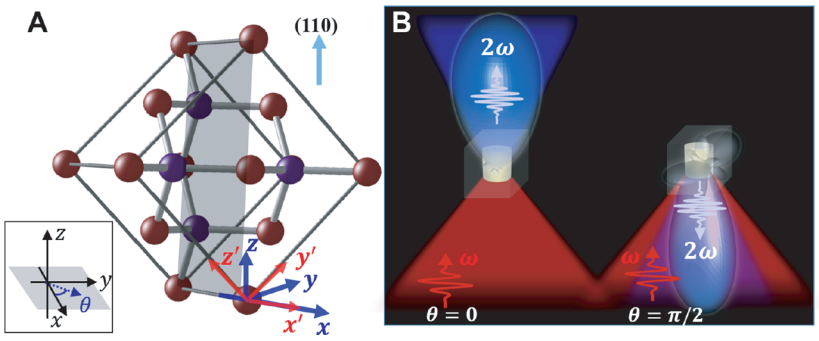

Figure 1. (A) Illustration of the (110) direction of the zinc-blende crystal structure. The laboratory and crystalline coordinates are defined as (x, y, z) and (x', y', z') with θ being the in-plane pump polarization angle with respect to the x-axis in the laboratory coordinate system. (B) Schematic of the all-optical unidirectional nonlinear emission switch via pump polarization control from the (110)-GaAs nanoantennas.

sensing optoelectronic devices.[15−17] However, there are two significant challenges that are impeding the transition of this technology to practical applications. The first challenge is to find the most appropriate materials with induced optical modes at the nanoscale, together with strong nonlinear properties, i.e., second and third order susceptibilities, to enhance the nonlinear conversion efficiency.[18] The second challenge is the lack of ability within the nonlinear nanoantennas to generate unidirectional nonlinear emission with switching capabilities. Unidirectional emission is highly desired for future nonlinear nanophotonics applications such as miniaturized multifunctional nonlinear elements and metadevices. Unidirectionality and switching have already been revealed in the linear regime, via simultaneous excitation and mutual interference of magnetic and electric multipoles inside the nanoparticles, so-called "Kerker"s type scattering.[19,20] However, in the nonlinear regime, the complexity of nonlinear tensors, as an additional degree of freedom, influences the emissions. To the best of our knowledge, the unidirectional light switch has not been demonstrated in the nonlinear regime yet.

To address the first challenge, initially, metallic nanoantennas have been extensively employed for the nonlinear processes due to the strong near-field enhancement arising from the coherent oscillations of conduction electrons near the surface of plasmonic structures.[2,21−36] However, the performance of nonlinear plasmonics is restricted by high Ohmic losses, small mode volumes, and low laser damage threshold. Subsequently, high-index dielectric nanostructures such as silicon (Si)[37] and germanium (Ge) nanoantennas,[38] which support both electric and magnetic Mie-type resonances, were considered as promising alternatives to overcome these limitations of nonlinear nanoplasmonics.[39−41] It has been shown that through exploiting different electric and magnetic multipolar resonances and taking advantage of various interferences between the optical modes, one can induce strong near-field enhancements and subsequently tailor the field distributions inside the nanostructures.[40,42,43] This capability was offered as a promising route to significantly facilitate the nonlinear interactions.[9,44−58]

In contrast to their strong third-order nonlinearities, Si and Ge do not possess bulk-mediated second-order nonlinearities due to their centrosymmetric crystalline structures. Thus, for the second-harmonic generation (SHG) processes, III−V semiconductors that typically have zinc-blende (ZB) crystal structure, such as GaAs,[59−66] AlGaAs,[67−71] and GaP,[72−74] have been explored based on their high-dielectric index and relatively strong second-order susceptibilities.[75] However, the drawback of ZB III−V nanoantennas is their complex nonlinear tensors. In the past few years, it has been widely discussed that due to the symmetry of the second-order bulk nonlinear susceptibility tensor, the corresponding SHG emission is usually suppressed in the normal direction by such nanoantennas, and mainly emitting in off-normal directions, making it difficult to collect the signal effectively even using a high numerical-aperture (NA) objective.[68] Several approaches have been employed to solve this hurdle, such as using asymmetric nanostructures,[76,77] tilting the pump beam,[78,79] and employing the coupling effect between nanostructures in the lattice.[80] However, all these techniques require complex nanostructuring or experimental implementation. All these approaches overlooked a common fact: based on the special nonlinear tensorial properties of ZB material, one can engineer the nonlinear properties via having the nanoantenna axis aligned along certain crystalline orientations of the III−V materials. Crystalline orientations are planes with corresponding Miller indices in the crystals. Indeed, all the above-mentioned studies were performed on ZB III−V nanoantennas grown along the (100) crystalline orientation which is the standard commercial wafer.[76−80] Recently, it has been demonstrated that nonzero nonlinear emissions in the normal direction can be achieved by employing (111)-grown GaAs nanoantennas,[81] whereby improved better forward directionalities compared to (100)-counterparts were presented. However, unidirectional emission of SHG from (100)- or (111)-grown ZB nanoantennas has not been demonstrated yet, due to the multipolar interference effect of the generated nonlinear multipoles with even values of azimuthal indices m.[68,69,81]

The second unresolved challenge of high-refractive-index nanoantennas in the nonlinear regime is the ability to tailor the nonlinear emission flexibly, particularly switching between forward and backward nonlinear emissions. It is worth notice that switching in the linear regime means that the incident and scattered lights have the same frequencies. Therefore, the scattered light is always accompanied by a large amount of incident light, which introduces a strong background signal.[82−84] On the other hand, switching in the nonlinear regime has the advantage of background-free detection as the harmonics are generated at different frequencies compared to the pump. Indeed, for practical applications in the nonlinear regime such as nonlinear sources, holograms, and quantum emitters, it is highly desirable to achieve switchable emission between forward and backward directions.[40,53,85] Despite these

DOI: 10.1021/acsnano.9b07117
ACS Nano 2020, 14, 1379−1389

well-known advantages, there has been no reported experimental demonstration for nonlinear switching yet.

In this paper, we present a solution to address both the above-mentioned drawbacks. By exploiting (110)-grown ZB GaAs nanoantennas, as shown in Figure 1A, we overcome the lack of unidirectional emission in ZB III−V semiconductors and experimentally reveal strong SHG emission with a vast control on the forward/backward (FB) ratio between them. By embedding the nanoantennas in optically transparent low-index material—a benzocyclobutene (BCB) layer—we have been able to experimentally examine forward and backward nonlinear emissions. First, we demonstrate that our (110)-grown nanoantennas enable suppressing forward or backward SHG emissions leading to the tunability of the FB ratio from 0.16 up to more than 45. Furthermore, we have managed to switch the unidirectional SHG forward emission to backward, and *vice versa* (see Figure 1B), by employing the interference between the noninear multipoles within (110)-grown nanoantennas. Manipulation of the interference can be achieved via controlling the pump polarization and/or the nanoantenna radii. Indeed, the capability of performing the nonlinear switching this way without any physical change on the nanoantenna geometries or environments has not been shown yet. Such a high degree of freedom in nonlinear light control has not been reported either in (100)- and (111)-ZB III−V or in Si/Ge nonlinear nanoantennas. Our results enable potential applications in nonlinear photonics, *e.g.*, optical switches, nanoscale nonlinear light routing elements, high-efficiency light sources, *etc.*

RESULTS AND DISCUSSION

Multipolar Analysis of SHG. During the SHG process, the directivity of nonlinear radiation is determined by the nonlinear multipolar interferences. Here, we will briefly discuss the specifics of the contribution from different multipoles to the SHG response from (110)-GaAs nanoantennas and clarify the nature of multipolar interference that can lead to directional nonlinear light emission.

The nonlinear response of nanoantennas made of GaAs (or AlGaAs) grown along different crystalline orientations significantly depends on the mutual orientation of the crystalline axes and pump polarization. Up to now, there have been several experimental studies demonstrating different nonlinear effects under resonant excitation of electric and magnetic dipolar modes in isolated nanoparticles, such as nonlinear generation of vector beams,[68] nonlinear optical magnetism,[69] and tailoring second-harmonic emission by rotation of beam polarization.[81] In the case of (100)-GaAs nanoantennas, the generated SH multipoles have even values of azimuthal indices $m = 0, \pm 2$ resulting in zero SHG radiation along the optical axis at normal incidence of the laser beam.[61,68,69] In contrast to (100)-GaAs nanoantennas, nonlinear currents in (111)-GaAs nanoantennas generate multipoles with both even and odd azimuthal indices m, demonstrating nonzero emission in the normal direction,[81] while the conversion efficiency is polarization-angle-independent. Here we show that (110)-GaAs nanoantennas generate multipoles with odd indices m only, which further allows maximizing the SHG forward and backward directionalities by rotation of the normally incident pump in-plane polarization.

The second-order susceptibility tensor of the ZB crystal structure contains only off-diagonal elements $\chi^{(2)}_{i'j'k'} = \chi^{(2)}$ with $i' \neq j' \neq k'$ and i', j', k' being the crystalline coordinates.[1] In the principal-axis system of the crystal, the ith component of the nonlinear electric polarization vector is given by[67,78]

$$P^{(2\omega)}_{i'} = \varepsilon_0 \chi^{(2)}_{i'j'k'} E^{(\omega)}_{j'} E^{(\omega)}_{k'} \tag{1}$$

where ε_0 is the vacuum permittivity and $E^{(\omega)}_{j'}$ and $E^{(\omega)}_{k'}$ are the electric field components at the pump frequency ω along the crystalline coordinates j' and k', respectively.

For (110)-grown ZB nanostructures, the relation between the crystalline and laboratory coordinate frames can be defined by the Euler rotation matrices (see the section "Theoretical analysis of SHG in (110)-grown zinc-blende materials" of the Supporting Information; see also Figure 1A). In the laboratory frame for a given electric field distribution $\mathbf{E}^{(\omega)}(x, y, z)$, the induced nonlinear polarization $\mathbf{P}^{(2\omega)}(x, y, z)$ can be calculated by transforming the electric field $\mathbf{E}^{(\omega)}(x, y, z)$ into the crystalline frame first, evaluating the nonlinear polarization in this frame, and then converting it back to the laboratory frame, using the inverse rotation transformation. The nonlinear polarization is given through the Cartesian electric field components obtained from the above expression eq 1 by applying coordinate transformations. In this way, the SH current density induced in (110)-GaAs nanoantenna can be written in the laboratory coordinate frame as (see also the section "Theoretical analysis of SHG in (110)-grown zinc-blende materials" of the Supporting Information):

$$J_x = 2i\omega\epsilon_0 d_{36}\{-E_y^2 \cos^3\alpha + E_x E_y \sin\alpha[3\cos 2\alpha + 1] + \cos\alpha[E_z^2 + (-3E_x^2 + 2E_y^2)\sin^2\alpha]\}$$

$$J_y = 2i\omega\epsilon_0 d_{36}[-2E_x E_y \cos^3\alpha - E_z^2 \sin\alpha + (2E_x^2 - E_y^2)\cos^2\alpha \sin\alpha + E_x^2 \sin^3\alpha]$$

$$J_z = 4i\omega\epsilon_0 d_{36} E_z[E_x \cos\alpha + E_y \sin\alpha]$$

using the contract notation $d_{36} = \frac{1}{2}\chi^{(2)}$,[1] and α is the angle between the laboratory coordinate axis x and the crystal coordinate axis x'.

By further investigating the multipolar composition of the generated SH field, we find that, in the spherical coordinate system, components of the nonlinear current comprise only odd values of the azimuthal indices m (as specified in Table 1 of the Supporting Information). The SH generated field is composed by multipoles with azimuthal indices $m = \pm 1, \pm 3$, and ± 5 only, whose interference may lead to prevalent SHG in the $\pm z$ out-of-plane directions (see Figure 2). This is confirmed by direct full-wave numerical simulations using COMSOL Multiphysics software for (110)-GaAs nanoantennas as employed in the experiment.

The simulations are performed for the GaAs nanoantenna with a nominal radius $r = 210$ nm and height $h = 400$ nm, placed in a homogeneous BCB medium (as our host medium) of a refractive index $n = 1.44$ at an excitation wavelength $\lambda_0 = 1450$ nm (which is the pump wavelength used in our experiment). Figure 2A,B shows a comparison of the SHG radiation from nanoantennas with different crystalline orientations as a function of the pump polarization rotation angle. The normalized SHG conversion efficiency is calculated through $\eta = \frac{P_{SHG}}{P_{pump}}$, where P_{SHG} is the measured total SHG emission power in the forward and backward directions and P_{pump} is the pump power illuminated on an individual disk surface area.[67,78,81] As demonstrated in ref 81, the total SHG

DOI: 10.1021/acsnano.9b07117
ACS Nano 2020, 14, 1379−1389

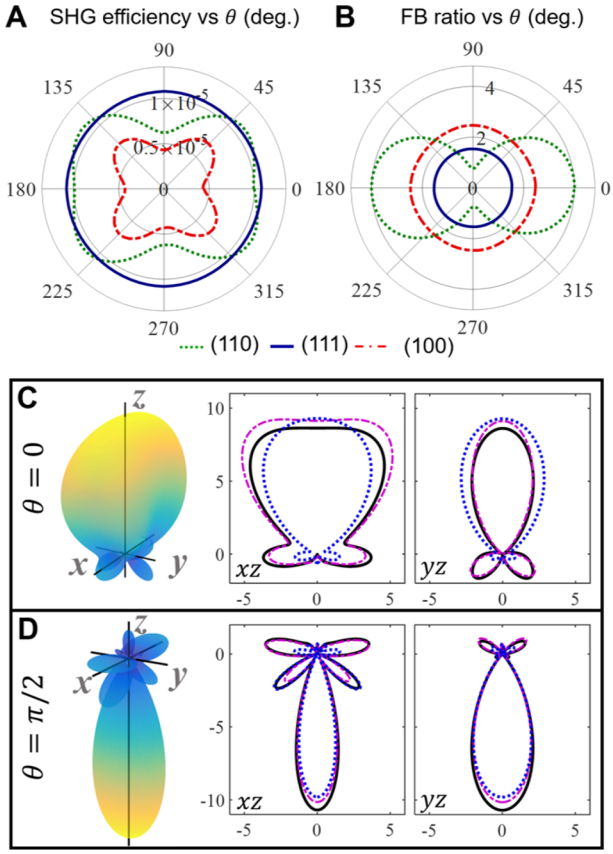

Figure 2. Polar plots visualizing dependencies of (A) total SHG efficiency and (B) forward/backward SH emission ratio on the pump polarization angle for different crystalline orientations. (C, D) The SH far-field diagrams and their cross sections in mutually orthogonal *xz* and *yz* planes (dark solid curve). The reconstructions of the radiation pattern are performed with multipoles up to *l* = 4 (pink dashed curve) and reduced sets of multipoles (blue dotted curve): electric dipoles (ED) $a_E(1, \pm1)$, electric (EQ) and magnetic (MQ) quadrupoles $a_{E,M}(2, \pm1)$ and electric hexadecapole (EH) $a_E(4, \pm1)$ at $\theta = 0$; ED $a_E(1, \pm1)$, electric (EO), and magnetic (MO) octupoles $a_{E,M}(3, \pm1)$ and EH $a_E(4, \pm1)$ at $\theta = \pi/2$.

power from (111)-GaAs nanoantennas remains constant. In the case of (100)-GaAs nanoantennas, SH power has a maximum at an angle of 45° and repeats every 90°.[61,68,69] Thus, the total conversion efficiency depends on the symmetry of the crystal plane normal to the propagation direction. For (100), (110), and (111) orientations, it exhibits 4-fold, 2-fold, and continuous rotational symmetries, respectively. We also examine the FB ratio defined here as the ratio of SHG power emitted into the *z*+ half-space to the SHG power emitted into *z*− half-space (see Figure 2B). In agreement with our predictions, the highest directionality corresponds to the (110)-GaAs nanoantenna. We find that, as a result of multipolar interference, the nanoantenna exhibits highly directional SHG for certain angles of pump polarization rotation, namely, $\theta = 0$ and $\theta = \pi/2$.

Next, we numerically determine which multipoles are responsible for these forward and backward emissions. The multipolar compositions of the SHG are different for these two directions. The numerically computed radiation patterns and their reconstructions with sets of leading multipoles are depicted in Figure 2C,D. These figures illustrate how the mutual interference of several multipolar spherical waves distinguished by azimuthal indices *m* and orbital indices *l* results in the emission directionality. By comparing the diagram of the far-field cross sections corresponding to the particular multipolar compositions and to compositions of all generated multipoles, we can see that, in the $\theta = 0$ case, the emission in the *z*+ direction is determined by interference of the electric dipoles (ED) $a_E(1, \pm1)$, electric (EQ) and magnetic (MQ) quadrupoles $a_{E,M}(2, \pm1)$, and electric hexadecapole (EH) $a_E(4, \pm1)$. In the $\theta = \pi/2$ case, we obtain emission in the *z*− direction due to interference of ED $a_E(1, \pm1)$ and electric (EO) and magnetic (MO) octupoles $a_{E,M}(3, \pm1)$ and EH $a_E(4, \pm1)$.

Linear Scattering and SHG Emission. To demonstrate the above-mentioned effects experimentally, we have designed and fabricated (110)-grown GaAs nanoantennas. The extinction coefficient κ is 0.11 at the SH wavelength (725 nm), leading to a penetration depth of $\delta_p = \lambda_{SH}/4\pi\kappa \approx 525$ nm at the SH wavelength, which exceeds the thickness of our nanoantennas (400 nm). Thus, the enhancement of the SHG in our case is derived from the Mie-type resonances at both the pump and the SH wavelengths. On the other hand, the linear scattering efficiency generally grows with the increase of the nanoantenna thickness (see Figure S1 of the Supporting Information). Therefore, the thickness of the GaAs nanoantennas (i.e., 400 nm) is optimal for both efficient excitation and outcoupling of the generated SH radiation. In our experiments, the height of our nanoantennas is fixed to be 400 nm. We consider the geometrical parameters of nanoantennas supporting low-order multipoles (up to quadrupoles) at the wavelength of the optical pump (1450 nm in our experiment), to enhance the near field inside the nanoantennas. Thus, we fabricate a set of individual nanoantennas with radii ranging from 150 to 350 nm which covers the low-order Mie resonant excitations at our pump wavelength. We implement a fabrication procedure where the GaAs nanoantennas are embedded in a transparent BCB layer, with an equivalent refractive index to glass, and placed on a glass substrate. This configuration is crucial to enable us to examine both the forward and backward nonlinear emissions. The fabrication steps are illustrated in Figure 3A (for more information about the fabrication procedure, see Figure S2 of the Supporting Information). The first important step, not shown in Figure 3, was the process of growth of a thin (110)-GaAs layer on a 20 nm aluminum arsenide (AlAs) buffer layer on a (110)-GaAs substrate using metal−organic chemical vapor deposition (MOCVD). Although the epitaxial growth on (100)-GaAs substrates is a well-established process, planar growth on (110)-substrates was a challenging step requiring high growth temperature, where the growth window was very narrow. For more details please see the Methods section. As can be seen in Figure 3A, the nanoantennas were then fabricated by employing electron-beam lithography followed by a dedicated transfer procedure developed in ref 68. Figure 3B shows the scanning electron microscopy (SEM) image of (i) a fabricated nanoantenna on the GaAs wafer before etching of the AlAs buffer layer and (ii) after transferring onto a thin glass substrate.

The multipolar decomposition of the linear scattering for different nanoantenna radii is illustrated in Figure 3C. The simulated linear scattering efficiency is defined as the scattering cross section C_{sca} normalized by the cross area of the nanoantenna πr^2: $Q_{sca} = C_{sca}/\pi r^2$. Due to the symmetry of

DOI: 10.1021/acsnano.9b07117
ACS Nano 2020, 14, 1379−1389

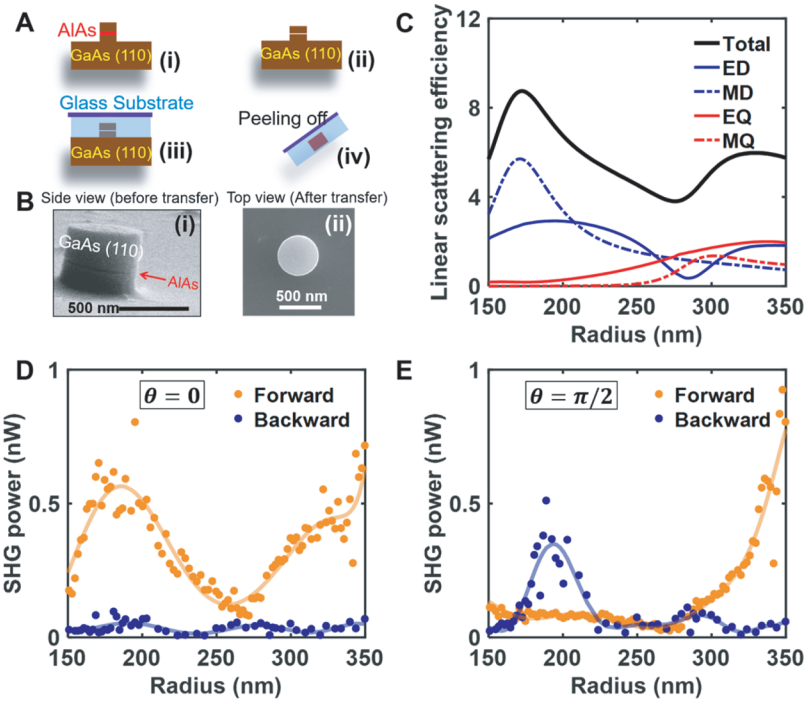

Figure 3. (A) Illustration of the fabrication procedure for the GaAs nanoantennas in a transparent medium: (i) GaAs nanoantennas defined on a GaAs wafer via electron-beam lithography and sequential etching. AlAs is grown as a sacrificial layer. (ii) Removal of the AlAs buffer layer by HF acid, followed by (iii) coating of a BCB layer, curing, and bonding it onto a thin glass substrate. (iv) Final sample containing the GaAs antennas, after peeling off. (B) Scanning electron microscope images: (i) side view of the etched GaAs antennas on the GaAs wafer and (ii) top view of the final sample on glass, after peeling off. (C) Calculated multipolar structure of the linear light scattering by GaAs nanoantennas with different nanoantenna radii under plane wave excitation at the wavelength of λ = 1450 nm, identical for (θ = 0) to (θ = 2π). (D) Experimentally measured forward and backward SHG emission power for different nanoantenna radii when the pump is *x*-polarized (see Figure 1A). (E) Experimentally measured forward and backward SHG emission intensity for different nanoantenna radii when the pump is *y*-polarized ($\theta = \pi/2$).

the nanoantennas, this graph is identical for any polarization direction (θ = 0) to (θ = 2π) of the normal incident wave. Two resonant peaks can be observed from the total scattering curve at nanoantenna radius around 170 and 320 nm, respectively. The first peak corresponds to the excitation of ED and magnetic dipole (MD) resonances, covering the radius range from 150 to 225 nm. The second resonant peak is attributed to a mixed contribution of EQ, MQ, ED, and MD excitations. The linear scattering spectra for several nanoantenna radii, as well as the near-field enhancement around the spectral positions of these resonant peaks, are plotted in Figures S3–S6 of the Supporting Information. As can be seen in Figure 3D,E, these enhanced near fields further improve the light–matter interactions and boost the nonlinear effects inside the nanoantennas. Experimentally, the fabricated GaAs nanoantennas have radii ranging from 150 to 350 nm with a step of 2 nm, covering the two targeted resonant positions at the pump wavelength. The nanoantennas are positioned 10 μm apart, which makes them optically isolated. The measured linear spectra of several nanoantennas clearly show the pronounced size-dependent resonance at the FW wavelength. It matches our simulation results which were obtained with the finite element method solver in COMSOL Multiphysics in the frequency domain (see Figure S7 of the Supporting Information).

We performed the SHG measurements for the fabricated GaAs nanoantennas with the radii from 150 to 350 nm and the thickness of 400 nm. We used a femtosecond laser with 10 mW average power, operating at the wavelength of 1450 nm with a 255 fs pulse width at the repetition rate of 80 MHz. The laser was focused by an objective with a numerical aperture (NA) of 0.7 onto the nanoantennas, with a 2 μm-beam-waist spot. Considering the light loss through each component before the sample (see the schematic of the nonlinear measurement setup in Figure S8 of the Supporting Information), the total power on the sample is around 1.6 mW, leading to the pump peak intensity value of I_0 of around 1.2 GW/cm^2. The beam waist of the focused laser on the sample was measured by imaging the focal area with a CCD camera, along with a Gaussian curve fitting. The SH signal in the backward direction was collected by the same objective. A NA = 0.8 objective was used to collect the forward SH emission (see the schematic of the nonlinear measurement setup in Figure S8 of the Supporting Information). Figure 3D,E demonstrates the measured forward and backward SHG emission power from the GaAs nanoantennas for different nanoantenna radii with a pump polarization angle being θ = 0 (*x*-polarized) and $\theta = \pi/2$ (*y*-polarized), respectively. Pronounced nonlinear emission enhancement is observed in the vicinity of the two resonant peak positions at the pump wavelength (see Figure 3C). Our normalized SHG conversion efficiency at the MD resonance, i.e., the peak at the diameter of 196 nm, is around 0.003% under our pump peak intensity of 1.2 GW/cm^2. Interestingly, when the pump polarization angle is θ = 0, for the SHG around the first resonant peak, a strong forward SH emission occurs with simultaneous suppression of the SH emission in the backward direction. On the other hand, for the pump polarization angle $\theta = \pi/2$, the improved nonlinear emission

DOI: 10.1021/acsnano.9b07117
ACS Nano 2020, 14, 1379–1389

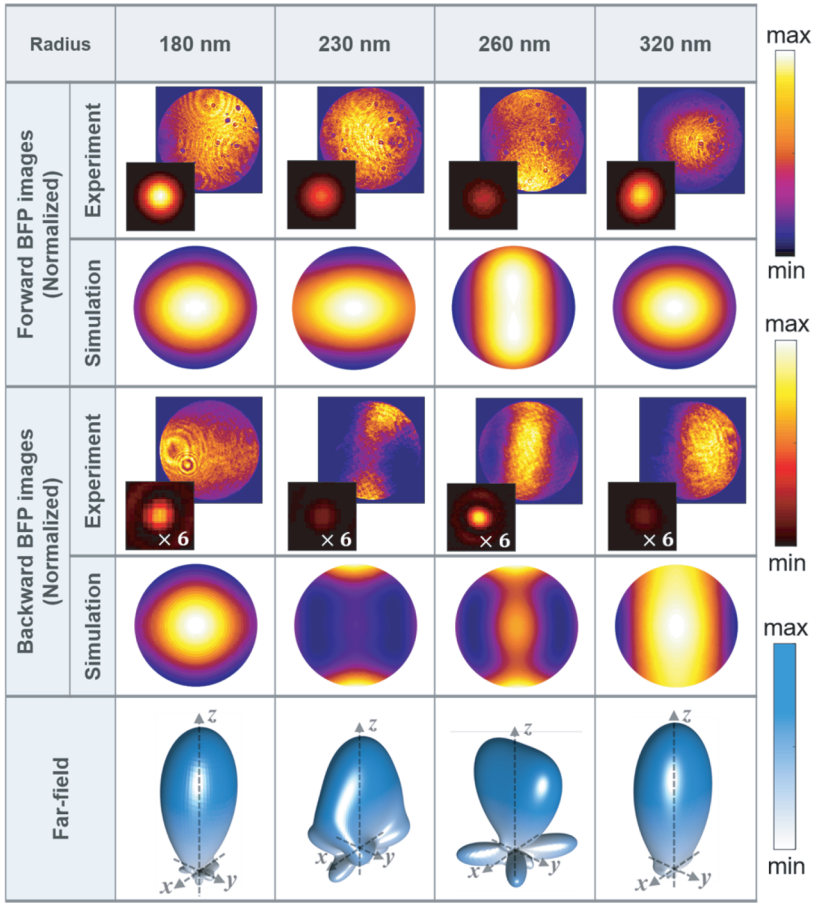

Figure 4. Experimental and theoretical SH emission patterns for nanoantennas with four different radii under a pump polarization angle of θ = 0. Experimental rows contain BFP (top) and real space SHG (bottom) images. The last (bottom) row shows the calculated SH radiation far-field patterns. Here, each BFP image is normalized to its respective maximum pixel value to give a good contrast, while the real-space images are under the same normalization to illustrate the SHG emission intensity variations for different nanoantenna radii.

takes place in the backward direction with a suppression of the forward nonlinear radiation. As described in the multipolar analysis of the SHG, this interesting feature of the nonlinear emission is attributed to the special second-order nonlinear tensor properties of (110)-orientated GaAs nanostructure, where both lower and higher order nonlinear multipoles are generated and are with odd indices m only. Therefore, the relative contribution of these nonlinear multipoles can be tuned via changing the pump polarization, and their interference further allows maximizing SHG forward or backward directionality (see also the section "Theoretical analysis of SHG in (110)-grown zinc-blende materials" and Figure S9 in the Supporting Information). These nonlinear multipolar interferences provide a robust tool to shape the nonlinear wavefront and obtain functional nonlinear directivity, as indicated in the rest of the paper. In order to get a deeper understanding, we next investigate the characteristic features of SHG emission directionalities from (110)-GaAs nanoantennas.

SHG Directionality. In order to study the directional propagation of the nonlinear emission, we employed back-focal-plane (BFP) imaging. We first consider the case of SHG emission for different nanoantenna' radii at a fixed pump polarization angle of θ = 0. By projecting the BFP images for the two objective lenses onto the cameras in the respective forward and backward directions, we experimentally retrieved the forward and backward SH radiation patterns on the basis of the NA of the objectives. Figure 4 shows the experimentally measured SHG emission directionalities for four different nanoantenna radii for fixed pump polarization angle θ = 0. The nanoantennas with the radii 180 nm, 230 nm, 260 nm, and 320 nm shown in Figure 4 were chosen because their radii correspond to the linear resonances of the multipolar excitation presented in the Figure 3C. To better understand the radiation properties of our nanoantennas, we also performed the corresponding numerical simulations. We calculated the SH far-field intensity distribution, which was projected onto the back-focal plane to obtain two-dimensional projections of SHG directionalities, in comparison with the experimental BFP images. As expected, since (110)-GaAs nanoantennas generate nonlinear multipoles with odd indices m, the SHG emissions from (110)-GaAs nanoantennas with different radii feature strong normal directionalities. This is an advantage to (111)-GaAs nanoantennas, where nonzero SHG emission in the forward or backward direction is strongly dependent on the nanoantenna dimensions.[81] These promising features of (110)-GaAs nanoantennas are also reflected by the real-space SHG intensity images shown in Figure 4 where the nonlinear light is confined into one spot in the center. It is worth mentioning that the slight differences between the theoretical and experimental results can be attributed to the small nonuniformity of the fabricated nanostructrures.

As mentioned above, an interesting feature of (110)-GaAs nanoantennas is the ability to provide various SHG FB ratios.

DOI: 10.1021/acsnano.9b07117
ACS Nano 2020, 14, 1379−1389

The relative contribution of different multipoles varies when changing the nanoantenna radii or rotating the pump polarization. The combination of both parameters leads to tuning of the directionality of the nonlinear emission. We then measured the forward and backward SHG power proportions (collected forward or backward SHG emission normalized to the total SHG emission power in both directions collected by the objectives) for different nanoantenna radii and for a pump polarized along the y direction, i.e., $\theta = \pi/2$. Figure 5 shows the

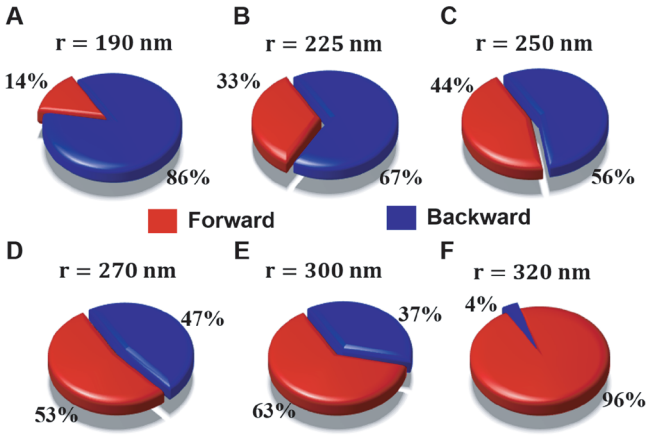

Figure 5. Experimentally measured forward and backward SHG power proportions for six different nanoantenna radii under a pump with polarization angle of $\theta = \pi/2$.

experimentally measured forward and backward SHG power proportions with varying nanoantenna radii. For r = 190 nm, most of the SHG emission goes into the backward direction, with a FB ratio of 0.16. With increasing nanoantenna radius, the proportion of forward SHG emission increases, while the proportion of the backward SHG emission decreases simultaneously. At a nanoantenna radius of r = 320 nm, the SHG emission mainly goes into the forward direction, with a FB ratio bigger than 20. A further investigation of the SHG FB ratio under different pump polarization angles θ is demonstrated in Figures S10 and S11 in the Supporting Information. Figures S10 and S11 demonstrate that the experimentally measured FB ratio can reach more than 45 from a single (110)-GaAs nanoantenna. Thus, we have obtained strong directional scattering of nonlinear emission from single nanoantennas and demonstrated that the nonlinear emission can be switched between forward and backward directions flexibly.

The most important feature of (110)-GaAs nanoantennas is that their directional nonlinear scattering can be tailored effectively by varying the nanoantenna radii or the pump polarization. This feature can be seen in the SHG radiation properties at a nanoantenna radius of r = 210 nm, where the simultaneous in-phase excitation of the ED and MD resonances of the same amplitude leads to the inhibition of backward radiation for the pump light, i.e., the first Kerker condition in the linear scattering process (see Figures S3 and S5 in the Supporting Information). Figure 6 shows the results of the nonlinear measurements for the nanoantenna radius of r = 210 nm. By rotating the pump polarization angle θ from 0 to $\pi/2$, the nonlinear emission is gradually switched from forward to backward: a strong forward emission can be seen around θ = 0 with a simultaneous suppression of the backward nonlinear emission. However, for $\theta = \pi/2$, enhanced nonlinear emission comes to existence in the backward direction with a suppression of the forward nonlinear radiation. In this way, our (110)-grown ZB semiconductor nanoantennas can act as tunable nonlinear "Huygens" sources. Such nonlinear nanoantennas provide a powerful tool for shaping and directing nonlinear signals, particularly in the case of metasurfaces (i.e., arrays of nanoresonators). For instance, this effect can be utilized for functional nonlinear metasurfaces, such as nonlinear mirrors, where the pump and harmonics radiations are routed into the opposite directions. It is worth mentioning that, for metasurfaces, the lattice periodicity would lead to a spectral shift of the resonance, as well as to the excitation of lattice resonances. A detailed description about the effect of

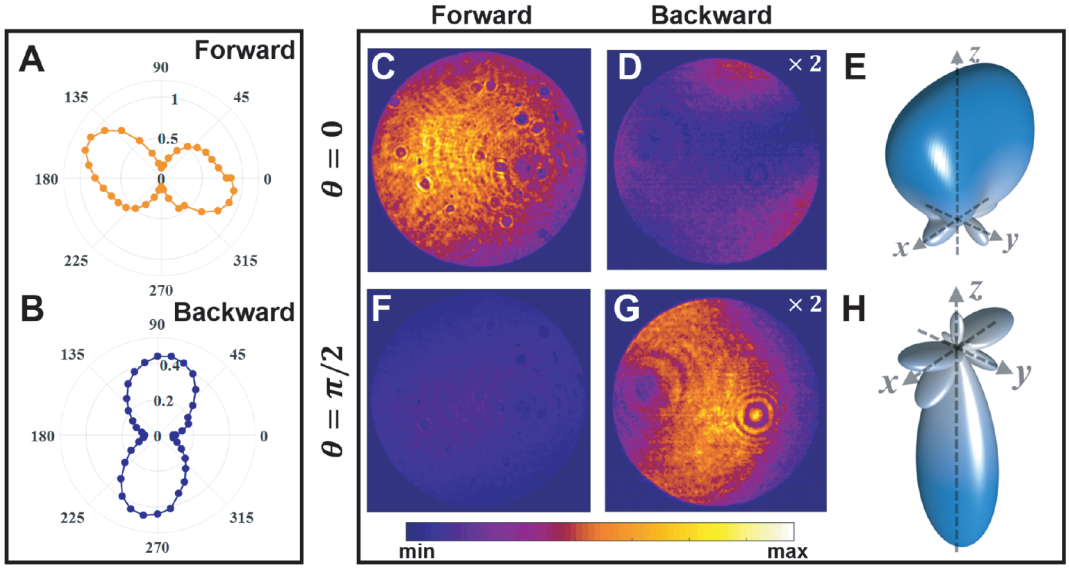

Figure 6. (A, B) Polar plots of the experimentally measured forward and backward SHG emission as a function of the pump polarization angle θ. (C–E and F–H) Measured forward and backward two-dimensional projections of directionalities and the calculated far-field pattern for the SHG emission when θ = 0 and when $\theta = \pi/2$, respectively. Here, the nanoantenna's radius is r = 210 nm.

DOI: 10.1021/acsnano.9b07117
ACS Nano 2020, 14, 1379–1389

periodicity can be seen in the section "Linear and nonlinear responses from (110)-GaAs nanoantenna metasurfaces" of the Supporting Information.

Our results clearly demonstrate the advantages of (110)-grown GaAs nanoantennas for SHG, as compared to (100)- and (111)-grown nanoantennas, in terms of directionality and switching. Furthermore, this study reveals the importance of the crystalline orientation in nonlinear nanoantennas, that has been mostly overlooked by researchers. Therefore, it can be followed by comprehensive studies on the crystalline orientation among other nonlinear nanoantennas, *e.g.*, AlGaAs, GaP, *etc*. Achieving all-optical nonlinear switching between forward and backward emission is a promising capability obtained through engineering special nonlinear tensorial properties of ZB GaAs nanoantennas. This is a fundamental study that can find broad potential applications in modern nanophotonics, such as tunable unidirectional nanoscale light sources, all-optical switching, optical signal modulation, and routing. Importantly, it can lead to generation of secure nonlinear holograms that can produce different images in forward and backward directions.

CONCLUSIONS

In conclusion, we demonstrate nonlinear switching between forward and backward SHG emissions via (110)-grown GaAs nanoantennas. Our GaAs nanoantennas, with engineered tensorial properties, were fabricated on a glass substrate. This characteristic enabled us to verify our designed forward and backward SHG emissions experimentally. First, via exploiting the right combination of crystalline orientation and the nonlinear multipolar effects, we experimentally obtained nonlinear emissions with significant FB ratio of over 45. Subsequently, we employed the pump polarization, as a versatile tool, to switch forward and backward SHG emissions to each other, robustly. Importantly, this switching has been achieved all-optically, without a need to introduce physical changes to the nanoantennas. Considering both the linear and nonlinear radiation properties from (110)-GaAs nanoantennas, our results can be directly employed to realize ultrathin nonlinear mirrors based on dielectric metasurfaces where the pump and harmonics radiation are routed into the opposite directions. Our findings offer a promising platform for realizing nonlinear nanophotonics technologies with applications in tunable nanoscale light sources.

METHODS

Sample Fabrication. We used metal–organic chemical vapor deposition (MOCVD) to grow 20 nm AlAs, followed by 400 nm GaAs on (110) GaAs wafers. The thin AlAs layer was used as an epitaxial liftoff layer. The deposition was carried out at 600 °C with a relatively low V/III ratio of 15. Trimethylgallium, trimethylaluminum, and arsine were used as the gallium, aluminum, and arsenic precursors, respectively. Patterned SiO_x masks were fabricated on the GaAs layer using a conventional e-beam lithography procedure. A SiO_x layer was deposited via plasma-enhanced chemical vapor deposition (PECVD). Then SiO_x disks were transferred to GaAs, AlAs, and GaAs wafers by the reactive ion etching (RIE) technique. SiO_x masks and AlAs layers were then removed by hydrofluoric acid, which resulted in having GaAs nanoantennas sitting on the GaAs wafer with minimum adhesion. The following step was the spin-coating of a 4 μm BCB layer on the sample and then its curing and bonding to a thin glass substrate (see Figure 3A). Finally, the glass substrate with the GaAs nanoantennas embedded in the BCB layer was peeled off from the main GaAs wafer.

Experimental Setup and Measurements. For the SHG intensity and back-focal plane image measurement, we used a home-built optical microscope setup (see the section "Experimental setup for nonlinear measurements" in the Supporting Information). A femtosecond laser at 1450 nm was focused with an NA = 0.7 objective and used to pump the sample. By imaging the focal area with a CCD camera, along with a Gaussian curve fitting, we estimated the beam waist of the focused laser on the sample around 2 μm. The SH signal was collected by the same objective in the backward direction. A dichroic mirror was used in front of the objective lens to direct the backward SH onto a camera. An objective with an NA = 0.8 was used to collect the SHG emission in the forward direction. A pair of confocal lenses were used to build a back-focal plane image of the SH radiation on the camera.

Numerical Calculations. The linear and nonlinear responses of our nanoantennas were modeled numerically using the finite-element method in COMSOL Multiphysics in the frequency domain. We assumed the undepleted pump field approximation and followed two steps to model the nonlinear response. The linear scattering at the fundamental wavelength was simulated, and the bulk nonlinear polarization induced inside the nanoantenna was obtained based on the transformation between the laboratory and crystalline coordinate frames (see section "Theoretical analysis of SHG in (110)-grown zinc-blende materials" in the Supporting Information). We then employed the obtained nonlinear polarization as a source for the electromagnetic simulation at the harmonic wavelength to obtain the generated SH field. For comparison with BFP images of the SH fields recovered experimentally with the objective, we used the Weyl representation, with assuming an aplanatic system. The calculated SH far-field intensity distribution was projected onto the back focal plane.[86−88] Also, we took into account the NA of the objective used in the experiment.

ASSOCIATED CONTENT

Supporting Information

The Supporting Information is available free of charge at https://pubs.acs.org/doi/10.1021/acsnano.9b07117.

> Theoretical analysis of SHG in (110)-grown zinc-blende materials; the linear scattering spectra for different nanoantenna thicknesses; the nanofabrication steps; the multipolar structures, near-field distributions, and far-field patterns for several nanoantenna radii; the experimental setup for nonlinear measurements; the multipolar structures of the SHG emission; the SHG emission polar plots for several different nanoantenna radii; and the linear and nonlinear responses from (110)-GaAs nanoantenna metasurfaces (PDF)

AUTHOR INFORMATION

Corresponding Authors

*(A.E.M.) E-mail: andrey.miroshnichenko@unsw.edu.au.
*(R.G.) E-mail: grange@phys.ethz.ch.
*(D.N.N.) E-mail: dragomir.neshev@anu.edu.au.

ORCID

Lei Xu: 0000-0001-9071-4311
Maria Timofeeva: 0000-0001-7192-8322
Khosro Zangeneh Kamali: 0000-0002-3160-737X
Andrey E. Miroshnichenko: 0000-0001-9607-6621
Rachel Grange: 0000-0001-7469-9756
Dragomir N. Neshev: 0000-0002-4508-8646
Mohsen Rahmani: 0000-0001-9268-4793

Author Contributions

⊥L.X. and G.S. contributed equally

DOI: 10.1021/acsnano.9b07117
ACS Nano 2020, 14, 1379−1389

Notes

The authors declare no competing financial interest.

ACKNOWLEDGMENTS

This work was supported by the Australian Research Council, the Swiss National Science Foundation Grants 150609 and 163916, and Ambizione Grant No. 179966, by the European Union's Horizon 2020 research and innovation program from the European Research Council under the Grant Agreement No. 714837 (Chi2-nano-oxides). M.R. sincerely appreciates funding from ARC Discover Early Career Research Fellowship (DE170100250) and The Australian Nanotechnology Network. The work of A.E.M. was supported by a UNSW Scientia Fellowship. D.A.S. acknowledges financial support from the ARC Early Career Researcher Award (DE190100430) and the Russian Foundation for Basic Research (Grant Nos. 18-02-00381 and 19-02-00261). I.V. was supported by the Foundation for the Advancement of Theoretical Physics and Mathematics BASIS. R.C.-M. acknowledges a grant from Consejo Nacional de Ciencia y Tecnología (CONACYT), Mexico. The authors acknowledge the use of the Australian National Fabrication Facility (ANFF), the ACT Node.

REFERENCES

(1) Boyd, R. W. *Nonlinear Optics*; Academic Press: New York, 2003.
(2) Kim, S.; Jin, J.; Kim, Y.-J.; Park, I.-Y.; Kim, Y.; Kim, S.-W. High-Harmonic Generation by Resonant Plasmon Field Enhancement. *Nature* **2008**, *453*, 757.
(3) Butet, J.; Duboisset, J.; Bachelier, G.; Russier-Antoine, I.; Benichou, E.; Jonin, C.; Brevet, P.-F. Optical Second Harmonic Generation of Single Metallic Nanoparticles Embedded in a Homogeneous Medium. *Nano Lett.* **2010**, *10*, 1717−1721.
(4) Semmlinger, M.; Tseng, M. L.; Yang, J.; Zhang, M.; Zhang, C.; Tsai, W.-Y.; Tsai, D. P.; Nordlander, P.; Halas, N. J. Vacuum Ultraviolet Light-Generating Metasurface. *Nano Lett.* **2018**, *18*, 5738−5743.
(5) Danckwerts, M.; Novotny, L. Optical Frequency Mixing at Coupled Gold Nanoparticles. *Phys. Rev. Lett.* **2007**, *98*, 026104.
(6) Rose, A.; Huang, D.; Smith, D. R. Nonlinear Interference and Unidirectional Wave Mixing in Metamaterials. *Phys. Rev. Lett.* **2013**, *110*, 063901.
(7) Zhang, Y.; Wen, F.; Zhen, Y.-R.; Nordlander, P.; Halas, N. J. Coherent Fano Resonances in a Plasmonic Nanocluster Enhance Optical Four-Wave Mixing. *Proc. Natl. Acad. Sci. U. S. A.* **2013**, *110*, 9215−9219.
(8) Nielsen, M. P.; Shi, X.; Dichtl, P.; Maier, S. A.; Oulton, R. F. Giant Nonlinear Response at a Plasmonic Nanofocus Drives Efficient Four-Wave Mixing. *Science* **2017**, *358*, 1179−1181.
(9) Yang, Y.; Wang, W.; Boulesbaa, A.; Kravchenko, I. I.; Briggs, D. P.; Puretzky, A.; Geohegan, D.; Valentine, J. Nonlinear Fano-Resonant Dielectric Metasurfaces. *Nano Lett.* **2015**, *15*, 7388−7393.
(10) Shcherbakov, M. R.; Liu, S.; Zubyuk, V. V.; Vaskin, A.; Vabishchevich, P. P.; Keeler, G.; Pertsch, T.; Dolgova, T. V.; Staude, I.; Brener, I.; et al. Ultrafast All-Optical Tuning of Direct-Gap Semiconductor Metasurfaces. *Nat. Commun.* **2017**, *8*, 17.
(11) Grinblat, G.; Berté, R.; Nielsen, M. P.; Li, Y.; Oulton, R. F.; Maier, S. A. Sub-20 fs All-Optical Switching in a Single Au-Clad Si Nanodisk. *Nano Lett.* **2018**, *18*, 7896−7900.
(12) Marino, G.; Solntsev, A. S.; Xu, L.; Gili, V. F.; Carletti, L.; Poddubny, A. N.; Rahmani, M.; Smirnova, D. A.; Chen, H.; Lemaître, A.; et al. Spontaneous Photon-Pair Generation from a Dielectric Nanoantenna. *Optica* **2019**, *6*, 1416−1422.
(13) Noginov, M.; Zhu, G.; Belgrave, A.; Bakker, R.; Shalaev, V.; Narimanov, E.; Stout, S.; Herz, E.; Suteewong, T.; Wiesner, U. Demonstration of a Spaser-Based Nanolaser. *Nature* **2009**, *460*, 1110.
(14) Totero Gongora, J. S.; Miroshnichenko, A. E.; Kivshar, Y. S.; Fratalocchi, A. Anapole Nanolasers for Mode-Locking and Ultrafast Pulse Generation. *Nat. Commun.* **2017**, *8*, 15535.
(15) Menon, V. M.; Deych, L. I.; Lisyansky, A. A. Nonlinear Optics: Towards Polaritonic Logic Circuits. *Nat. Photonics* **2010**, *4*, 345−346.
(16) van Sark, W. G.; de Wild, J.; Rath, J. K.; Meijerink, A.; Schropp, R. E. Upconversion in Solar Cells. *Nanoscale Res. Lett.* **2013**, *8*, 81.
(17) Rodrigues, S. P.; Lan, S.; Kang, L.; Cui, Y.; Cai, W. Nonlinear Imaging and Spectroscopy of Chiral Metamaterials. *Adv. Mater.* **2014**, *26*, 6157−6162.
(18) Rahmani, M.; Leo, G.; Brener, I.; Zayats, A. V.; Maier, S. A.; De Angelis, C.; Tan, H.; Gili, V. F.; Karouta, F.; Oulton, R.; et al. Nonlinear Frequency Conversion in Optical Nanoantennas and Metasurfaces: Materials Evolution and Fabrication. *Opto-Electron. Adv.* **2018**, *1*, 180021.
(19) Fu, Y. H.; Kuznetsov, A. I.; Miroshnichenko, A. E.; Yu, Y. F.; Luk'yanchuk, B. Directional Visible Light Scattering by Silicon Nanoparticles. *Nat. Commun.* **2013**, *4*, 1527.
(20) Paniagua-Domínguez, R.; Yu, Y. F.; Miroshnichenko, A. E.; Krivitsky, L. A.; Fu, Y. H.; Valuckas, V.; Gonzaga, L.; Toh, Y. T.; Kay, A. Y. S.; Luk'yanchuk, B.; et al. Generalized Brewster Effect in Dielectric Metasurfaces. *Nat. Commun.* **2016**, *7*, 10362.
(21) Maier, S. A. *Plasmonics: Fundamentals and Applications*; Springer Science & Business Media: Berlin, 2007.
(22) Knight, M. W.; Wu, Y.; Lassiter, J. B.; Nordlander, P.; Halas, N. J. Substrates Matter: Influence of an Adjacent Dielectric on an Individual Plasmonic Nanoparticle. *Nano Lett.* **2009**, *9*, 2188−2192.
(23) Lippitz, M.; van Dijk, M. A.; Orrit, M. Third-Harmonic Generation from Single Gold Nanoparticles. *Nano Lett.* **2005**, *5*, 799−802.
(24) Luk'yanchuk, B.; Zheludev, N. I.; Maier, S. A.; Halas, N. J.; Nordlander, P.; Giessen, H.; Chong, C. T. The Fano Resonance in Plasmonic Nanostructures and Metamaterials. *Nat. Mater.* **2010**, *9*, 707.
(25) Zhang, S.; Bao, K.; Halas, N. J.; Xu, H.; Nordlander, P. Substrate-Induced Fano Resonances of A Plasmonic Nanocube: A Route to Increased-Sensitivity Localized Surface Plasmon Resonance Sensors Revealed. *Nano Lett.* **2011**, *11*, 1657−1663.
(26) Lassiter, J. B.; Sobhani, H.; Fan, J. A.; Kundu, J.; Capasso, F.; Nordlander, P.; Halas, N. J. Fano Resonances in Plasmonic Nanoclusters: Geometrical and Chemical Tunability. *Nano Lett.* **2010**, *10*, 3184−3189.
(27) Klimov, V. *Nanoplasmonics: Fundamentals and Applications*; Pan Stanford: Singapore, 2012.
(28) Hanke, T.; Cesar, J.; Knittel, V.; Trügler, A.; Hohenester, U.; Leitenstorfer, A.; Bratschitsch, R. Tailoring Spatiotemporal Light Confinement in Single Plasmonic Nanoantennas. *Nano Lett.* **2012**, *12*, 992−996.
(29) Hentschel, M.; Utikal, T.; Giessen, H.; Lippitz, M. Quantitative Modeling of the Third Harmonic Emission Spectrum of Plasmonic Nanoantennas. *Nano Lett.* **2012**, *12*, 3778−3782.
(30) Aouani, H.; Rahmani, M.; Navarro-Cía, M.; Maier, S. A. Third-Harmonic-Upconversion Enhancement from a Single Semiconductor Nanoparticle Coupled to a Plasmonic Antenna. *Nat. Nanotechnol.* **2014**, *9*, 290−294.
(31) Meinzer, N.; Barnes, W. L.; Hooper, I. R. Plasmonic Meta-Atoms and Metasurfaces. *Nat. Photonics* **2014**, *8*, 889.
(32) Ahmadivand, A.; Gerislioglu, B.; Pala, N. Active Control over the Interplay between the Dark and Hidden Sides of Plasmonics Using Metallodielectric Au−Ge2Sb2Te5 Unit Cells. *J. Phys. Chem. C* **2017**, *121*, 19966.
(33) Ahmadivand, A.; Semmlinger, M.; Dong, L.; Gerislioglu, B.; Nordlander, P.; Halas, N. J. Toroidal Dipole-Enhanced Third Harmonic Generation of Deep Ultraviolet Light Using Plasmonic Meta-Atoms. *Nano Lett.* **2019**, *19*, 605−611.
(34) Kim, K.-H.; Rim, W.-S. Strongly Resonant Metasurfaces Supported by Reflective Substrates for Highly Efficient Second-and High-Harmonic Generations with Ultralow Pump Intensity. *Phys. Chem. Chem. Phys.* **2019**, *21*, 19076−19082.

DOI: 10.1021/acsnano.9b07117
ACS Nano 2020, 14, 1379−1389

(35) Rim, W.-S.; Kim, K.-H. Broadband Visible-Near Infrared and Deep Ultraviolet Generation by Four-Wave Mixing and High-Order Stimulated Raman Scattering From Hybrid Metasurfaces of Plasmonic Nanoantennae and Raman Active Nanoparticles. *Phys. Chem. Chem. Phys.* **2019**, *21*, 26615−26620.
(36) Kim, K.-H.; Rim, W.-S. Composite-Assisted Phase-Matching: Efficient Wavelength Conversion in Nonlinear Optical Composite Materials Containing Metal Nanoparticles. *Ann. Phys. (Berlin, Ger.)* **2019**, *531*, 1800156.
(37) Garcia-Etxarri, A.; Gómez-Medina, R.; Froufe-Perez, L. S.; Lopez, C.; Chantada, L.; Scheffold, F.; Aizpurua, J.; Nieto-Vesperinas, M.; Sáenz, J. J. Strong Magnetic Response of Submicron Silicon Particles in the Infrared. *Opt. Express* **2011**, *19*, 4815−4826.
(38) Gomez-Medina, R.; Garcia-Camara, B.; Suárez-Lacalle, I.; González, F.; Moreno, F.; Nieto-Vesperinas, M.; Sáenz, J. J. Electric and Magnetic Dipolar Response of Germanium Nanospheres: Interference Effects, Scattering Anisotropy, and Optical Forces. *J. Nanophotonics* **2011**, *5*, 053512.
(39) Kuznetsov, A. I.; Miroshnichenko, A. E.; Fu, Y. H.; Zhang, J.; Luk'yanchuk, B. Magnetic Light. *Sci. Rep.* **2012**, *2*, 492.
(40) Kuznetsov, A. I.; Miroshnichenko, A. E.; Brongersma, M. L.; Kivshar, Y. S.; Luk'yanchuk, B. Optically Resonant Dielectric Nanostructures. *Science* **2016**, *354*, aag2472.
(41) Staude, I.; Pertsch, T.; Kivshar, Y. S. All-Dielectric Resonant Meta-Optics Lightens Up. *ACS Photonics* **2019**, *6*, 802−814.
(42) Kamenetskii, E.; Sadreev, A.; Miroshnichenko, A. *Fano Resonances in Optics and Microwaves*; Springer: New York, 2018.
(43) Zangeneh Kamali, K.; Xu, L.; Ward, J.; Wang, K.; Li, G.; Miroshnichenko, A. E.; Neshev, D.; Rahmani, M. Reversible Image Contrast Manipulation with Thermally Tunable Dielectric Meta-surfaces. *Small* **2019**, *15*, 1805142.
(44) Shcherbakov, M. R.; Neshev, D. N.; Hopkins, B.; Shorokhov, A. S.; Staude, I.; Melik-Gaykazyan, E. V.; Decker, M.; Ezhov, A. A.; Miroshnichenko, A. E.; Brener, I.; et al. Enhanced Third-Harmonic Generation in Silicon Nanoparticles Driven by Magnetic Response. *Nano Lett.* **2014**, *14*, 6488−6492.
(45) Smirnova, D.; Kivshar, Y. S. Multipolar Nonlinear Nano-photonics. *Optica* **2016**, *3*, 1241.
(46) Shorokhov, A. S.; Melik-Gaykazyan, E. V.; Smirnova, D. A.; Hopkins, B.; Chong, K. E.; Choi, D.-Y.; Shcherbakov, M. R.; Miroshnichenko, A. E.; Neshev, D. N.; Fedyanin, A. A.; et al. Multifold Enhancement of Third-Harmonic Generation in Dielectric Nanoparticles Driven by Magnetic Fano Resonances. *Nano Lett.* **2016**, *16*, 4857−4861.
(47) Grinblat, G.; Li, Y.; Nielsen, M. P.; Oulton, R. F.; Maier, S. A. Enhanced Third Harmonic Generation in Single Germanium Nanodisks Excited at the Anapole Mode. *Nano Lett.* **2016**, *16*, 4635−4640.
(48) Grinblat, G.; Li, Y.; Nielsen, M. P.; Oulton, R. F.; Maier, S. A. Degenerate Four-Wave Mixing in a Multiresonant Germanium Nanodisk. *ACS Photonics* **2017**, *4*, 2144−2149.
(49) Shibanuma, T.; Grinblat, G.; Albella, P.; Maier, S. A. Efficient Third Harmonic Generation from Metal−Dielectric Hybrid Nano-antennas. *Nano Lett.* **2017**, *17*, 2647−2651.
(50) Krasnok, A.; Tymchenko, M.; Alù, A. Nonlinear Metasurfaces: A Paradigm Shift in Nonlinear Optics. *Mater. Today* **2018**, *21*, 8−21.
(51) Xu, L.; Rahmani, M.; Zangeneh Kamali, K.; Lamprianidis, A.; Ghirardini, L.; Sautter, J.; Camacho-Morales, R.; Chen, H.; Parry, M.; Staude, I.; et al. Boosting Third-Harmonic Generation by a Mirror-Enhanced Anapole Resonator. *Light: Sci. Appl.* **2018**, *7*, 44.
(52) Kim, K.-H.; Rim, W.-S. Anapole Resonances Facilitated by High-Index Contrast between Substrate and Dielectric Nanodisk Enhance Vacuum Ultraviolet Generation. *ACS Photonics* **2018**, *5*, 4769−4775.
(53) Sain, B.; Meier, C.; Zentgraf, T. Nonlinear Optics in All-Dielectric Nanoantennas and Metasurfaces: A Review. *Adv. Photon.* **2019**, *1*, 024002.
(54) Colom, R.; Xu, L.; Marini, L.; Bedu, F.; Ozerov, I.; Begou, T.; Lumeau, J.; Miroshnishenko, A. E.; Neshev, D. N.; Kuhlmey, B.; et al. Enhanced Four-Wave Mixing in Doubly Resonant Si Nanoresonators. *ACS Photonics* **2019**, *6*, 1295−1301.
(55) Xu, L.; Zangeneh Kamali, K.; Huang, L.; Rahmani, M.; Smirnov, A.; Camacho-Morales, R.; Ma, Y.; Zhang, G.; Woolley, M.; Neshev, D.; et al. Dynamic Nonlinear Image Tuning through Magnetic Dipole Quasi-BIC Ultrathin Resonators. *Adv. Sci.* **2019**, *6*, 1802119.
(56) Reineke, B.; Sain, B.; Zhao, R.; Carletti, L.; Liu, B.; Huang, L.; De Angelis, C.; Zentgraf, T. Silicon Metasurfaces for Third Harmonic Geometric Phase Manipulation and Multiplexed Holography. *Nano Lett.* **2019**, *19*, 6585−6591.
(57) Semmlinger, M.; Zhang, M.; Tseng, M. L.; Huang, T.-T.; Yang, J.; Tsai, D. P.; Nordlander, P.; Halas, N. J. Generating Third Harmonic Vacuum Ultraviolet Light with a TiO_2 Metasurface. *Nano Lett.* **2019**, *19*, 8972.
(58) Kroychuk, M. K.; Yagudin, D. F.; Shorokhov, A. S.; Smirnova, D. A.; Volkovskaya, I. I.; Shcherbakov, M. R.; Shvets, G.; Kivshar, Y. S.; Fedyanin, A. A. Tailored Nonlinear Anisotropy in Mie-Resonant Dielectric Oligomers. *Adv. Opt. Mater.* **2019**, *7*, 1900447.
(59) Timofeeva, M.; Bouravleuv, A.; Cirlin, G.; Shtrom, I.; Soshnikov, I.; Reig Escalé, M.; Sergeyev, A.; Grange, R. Polar Second-Harmonic Imaging to Resolve Pure and Mixed Crystal Phases along GaAs Nanowires. *Nano Lett.* **2016**, *16*, 6290−6297.
(60) Gili, V. F.; Carletti, L.; Locatelli, A.; Rocco, D.; Finazzi, M.; Ghirardini, L.; Favero, I.; Gomez, C.; Lemaître, A.; Celebrano, M.; et al. Monolithic AlGaAs Second-Harmonic Nanoantennas. *Opt. Express* **2016**, *24*, 15965.
(61) Frizyuk, K.; Volkovskaya, I.; Smirnova, D.; Poddubny, A.; Petrov, M. Second-Harmonic Generation in Mie-Resonant Dielectric Nanoparticles Made of Noncentrosymmetric Materials. *Phys. Rev. B: Condens. Matter Mater. Phys.* **2019**, *99*, 075425.
(62) Smirnova, D.; Smirnov, A. I.; Kivshar, Y. S. Multipolar Second-Harmonic Generation by Mie-Resonant Dielectric Nanoparticles. *Phys. Rev. A: At., Mol., Opt. Phys.* **2018**, *97*, 013807.
(63) Timofeeva, M.; Lang, L.; Timpu, F.; Renaut, C.; Bouravleuv, A.; Shtrom, I.; Cirlin, G.; Grange, R. Anapoles in Free-Standing III−V Nanodisks Enhancing Second-Harmonic Generation. *Nano Lett.* **2018**, *18*, 3695−3702.
(64) Liu, S.; Vabishchevich, P. P.; Vaskin, A.; Reno, J. L.; Keeler, G. A.; Sinclair, M. B.; Staude, I.; Brener, I. An All-Dielectric Metasurface as a Broadband Optical Frequency Mixer. *Nat. Commun.* **2018**, *9*, 2507.
(65) Löchner, F. J.; Fedotova, A. N.; Liu, S.; Keeler, G. A.; Peake, G. M.; Saravi, S.; Shcherbakov, M. R.; Burger, S.; Fedyanin, A. A.; Brener, I.; et al. Polarization-Dependent Second Harmonic Diffraction from Resonant GaAs Metasurfaces. *ACS Photonics* **2018**, *5*, 1786−1793.
(66) Zubyuk, V. V.; Vabishchevich, P. P.; Shcherbakov, M. R.; Shorokhov, A. S.; Fedotova, A. N.; Liu, S.; Keeler, G.; Dolgova, T. V.; Staude, I.; Brener, I.; et al. Low-Power Absorption Saturation in Semiconductor Metasurfaces. *ACS Photonics* **2019**, *6*, 2797−2806.
(67) Carletti, L.; Locatelli, A.; Stepanenko, O.; Leo, G.; De Angelis, C. Enhanced Second-Harmonic Generation from Magnetic Resonance in AlGaAs Nanoantennas. *Opt. Express* **2015**, *23*, 26544.
(68) Camacho-Morales, R.; Rahmani, M.; Kruk, S.; Wang, L.; Xu, L.; Smirnova, D. A.; Solntsev, A. S.; Miroshnichenko, A.; Tan, H. H.; Karouta, F.; et al. Nonlinear Generation of Vector Beams from AlGaAs Nanoantennas. *Nano Lett.* **2016**, *16*, 7191−7197.
(69) Kruk, S. S.; Camacho-Morales, R.; Xu, L.; Rahmani, M.; Smirnova, D. A.; Wang, L.; Tan, H. H.; Jagadish, C.; Neshev, D. N.; Kivshar, Y. S. Nonlinear Optical Magnetism Revealed by Second-Harmonic Generation in Nanoantennas. *Nano Lett.* **2017**, *17*, 3914−3918.
(70) Liu, S.; Vaskin, A.; Addamane, S.; Leung, B.; Tsai, M.-C.; Yang, Y.; Vabishchevich, P. P.; Keeler, G. A.; Wang, G.; He, X.; et al. Light-Emitting Metasurfaces: Simultaneous Control of Spontaneous Emission and Far-Field Radiation. *Nano Lett.* **2018**, *18*, 6906−6914.
(71) Gigli, C.; Marino, G.; Suffit, S.; Patriarche, G.; Beaudoin, G.; Pantzas, K.; Sagnes, I.; Favero, I.; Leo, G. Polarization-and

DOI: 10.1021/acsnano.9b07117
ACS Nano 2020, 14, 1379−1389

Diffraction-Controlled Second-Harmonic Generation from Semiconductor Metasurfaces. *J. Opt. Soc. Am. B* **2019**, *36*, E55−E64.
(72) Sanatinia, R.; Swillo, M.; Anand, S. Surface Second-Harmonic Generation from Vertical GaP Nanopillars. *Nano Lett.* **2012**, *12*, 820−826.
(73) Cambiasso, J.; Grinblat, G.; Li, Y.; Rakovich, A.; Cortés, E.; Maier, S. A. Bridging the Gap between Dielectric Nanophotonics and the Visible Regime with Effectively Lossless Gallium Phosphide Antennas. *Nano Lett.* **2017**, *17*, 1219−1225.
(74) Rocco, D.; De Angelis, C.; de Ceglia, D.; Carletti, L.; Scalora, M.; Vincenti, M. Dielectric Nanoantennas on Epsilon-Near-Zero Substrates: Impact of Losses on Second Order Nonlinear Processes. *Opt. Commun.* **2020**, *456*, 124570.
(75) Liu, S.; Keeler, G. A.; Reno, J. L.; Sinclair, M. B.; Brener, I. III−V Semiconductor Nanoresonators - A New Strategy for Passive, Active, and Nonlinear All-Dielectric Metamaterials. *Adv. Opt. Mater.* **2016**, *4*, 1457−1462.
(76) Xu, L.; Rahmani, M.; Smirnova, D.; Zangeneh Kamali, K. Z.; Zhang, G.; Neshev, D.; Miroshnichenko, A. Highly-Efficient Longitudinal Second-Harmonic Generation from Doubly-Resonant AlGaAs Nanoantennas. *Photonics* **2018**, *5*, 29.
(77) Ghirardini, L.; Marino, G.; Gili, V. F.; Favero, I.; Rocco, D.; Carletti, L.; Locatelli, A.; De Angelis, C.; Finazzi, M.; Celebrano, M.; et al. Shaping the Nonlinear Emission Pattern of a Dielectric Nanoantenna by Integrated Holographic Gratings. *Nano Lett.* **2018**, *18*, 6750−6755.
(78) Carletti, L.; Locatelli, A.; Neshev, D.; De Angelis, C. Shaping the Radiation Pattern of Second-Harmonic Generation from AlGaAs Dielectric Nanoantennas. *ACS Photonics* **2016**, *3*, 1500−1507.
(79) Carletti, L.; Marino, G.; Ghirardini, L.; Gili, V. F.; Rocco, D.; Favero, I.; Locatelli, A.; Zayats, A. V.; Celebrano, M.; Finazzi, M.; et al. Nonlinear Goniometry by Second-Harmonic Generation in AlGaAs Nanoantennas. *ACS Photonics* **2018**, *5*, 4386−4392.
(80) Marino, G.; Gigli, C.; Rocco, D.; Lemaître, A.; Favero, I.; De Angelis, C.; Leo, G. Zero-Order Second Harmonic Generation from AlGaAs-on-Insulator Metasurfaces. *ACS Photonics* **2019**, *6*, 1226−1231.
(81) Sautter, J. D.; Xu, L.; Miroshnichenko, A. E.; Lysevych, M.; Volkovskaya, I.; Smirnova, D. A.; Camacho-Morales, R.; Zangeneh Kamali, K.; Karouta, F.; Vora, K.; et al. Tailoring Second-Harmonic Emission from (111)-GaAs Nanoantennas. *Nano Lett.* **2019**, *19*, 3905−3911.
(82) Bohren, C. F.; Huffman, D. R. *Absorption and Scattering of Light by Small Particles*; John Wiley & Sons: New York, 2008.
(83) Novotny, L.; van Hulst, N. Antennas for Light. *Nat. Photonics* **2011**, *5*, 83−90.
(84) Koenderink, A. F.; Alu, A.; Polman, A. Nanophotonics: Shrinking Light-Based Technology. *Science* **2015**, *348*, 516−521.
(85) Keren-Zur, S.; Michaeli, L.; Suchowski, H.; Ellenbogen, T. Shaping Light with Nonlinear Metasurfaces. *Adv. Opt. Photonics* **2018**, *10*, 309−353.
(86) Weyl, H. Ausbreitung Elektromagnetischer Wellen über Einem Ebenen Leiter. *Ann. Phys. (Berlin, Ger.)* **1919**, *365*, 481−500.
(87) Lieb, M. A.; Zavislan, J. M.; Novotny, L. Single-Molecule Orientations Determined by Direct Emission Pattern Imaging. *J. Opt. Soc. Am. B* **2004**, *21*, 1210−1215.
(88) Novotny, L.; Hecht, B. *Principles of Nano-Optics*; Cambridge University Press: New York, 2006.

DOI: 10.1021/acsnano.9b07117
ACS Nano 2020, 14, 1379−1389